PAPER

Check for updates

Ni-doping effects on formation and migration of oxygen vacancies in SrFe$_{1-x}$Ni$_x$O$_{3-\delta}$ oxygen carriers

Ting Jia, ID *[a] Yinuo Hao,[a] Hua Hao ID [a] and Zhi Zeng[bc]

Ni is a promising B-site doping element capable of improving the oxygen carrier performance of SrFeO$_3$ perovskite. In this work, the effect of Ni doping on the formation and migration of oxygen vacancies in SrFe$_{1-x}$Ni$_x$O$_{3-\delta}$ ($x = 0$, 0.0625, 0.125, 0.1875, and 0.25) is investigated using density functional theory calculations. Our results show that the oxygen vacancies formed from Ni−O−Fe chains exhibit lower formation energy (E_f) compared to those from Fe−O−Fe chains in each doping system. Additionally, E_f generally decreases with an increase of Ni content. This Ni-promoted formation of V$_O$ is attributed to three factors: weakened Ni−O bonding, the closure of O-2p states to the Fermi level by Ni−O hybridization, and Ni^{3+} decreasing the positive charges to be compensated by V$_O$ formation. Due to these multiple advantages, a modest Ni doping of $x = 0.25$ can induce a higher P_{O_2} and a lower T compared to the relatively larger Co doping of $x = 0.5$, thermodynamically. Kinetically, Ni-doping appears to be a disadvantage as it hinders oxygen migration, due to a higher oxygen migration barrier through SrSrNi compared to the SrSrFe pathway. However, the overall oxygen ion conduction would not be significantly influenced by hopping through a nearby pathway of SrSrFe with a low migration barrier in a system doped with a small amount of Ni. In a word, a small amount of Ni doping has an advantage over Co doping in terms of enhancing the oxygen carrier performance of the parent SrFeO$_3$ system.

1. Introduction

Metal-oxide perovskites ABO$_{3-\delta}$ are a type of oxygen-carrier material, which can reversibly store and release oxygen by changing their oxygen content and structure under different partial oxygen pressures of the surrounding atmosphere and/or temperature. They have potential applications in energy storage, catalysis, gas sensing, and chemical looping.[1–4] Oxygen vacancy formation and migration are essential properties of oxygen carriers. Among a large number of possible non-stoichiometric perovskites, SrFeO$_{3-\delta}$ with a large fluctuation of oxygen non-stoichiometric values over a wide temperature range ($\delta = 0$ to ~0.5 from 0 to 1400 °C)[5–7] has been identified as a promising oxygen carrier for air separation.[8–11] However, it is noted that a pure SrFeO$_{3-\delta}$ system has some issues in limited oxygen carrying capacity, releasing oxygen at a very low oxygen partial pressure and poor stability under a pure CO or CO$_2$ atmosphere, etc.

Therefore, many efforts have been made to enhance its chemical stability and improve its performance by A/B-site substitution.[2,12–20] In particular, 3d transition metals are good candidates for B-site dopants, since these ions have similar

ionic radii to that of Fe and may take part in redox reactions. Demizu et al. have reported that SrFe$_{1-x}$Ti$_x$O$_{3-\delta}$ has a more stable perovskite structure under reducing conditions and exhibits faster oxygen storage/release rates compared to the unsubstituted SrFeO$_{3-\delta}$.[21] Mn and Co are neighboring atoms of Fe in the periodic table and thus are considered as the preferred dopants for the Fe site. It has been found that the crystal structure of SrFe$_{1-x}$Mn$_x$O$_{3-\delta}$ is stable during oxygen desorption and Fe ions are more easily reduced.[22] Our previous work on the optimal Co-doping of SrFe$_{1-x}$Co$_x$O$_{3-\delta}$ showed that Co-doping can promote oxygen release and revealed the optimal Co-doping value and the promotion mechanism.[23]

It has been reported that oxygen vacancy formation becomes easier as the radius of the B-site cation decreases.[24–26] Since Ni is the next nearest neighbor of Fe and has a smaller ionic radius, using Ni as a B-site dopant is very likely to improve the oxygen-carrier performance of SrFeO$_{3-\delta}$. In particular, our recent work has shown that low Ni doping in Sr$_{1-x}$Ca$_x$FeO$_3$ can promote oxygen vacancy formation.[14] Therefore, in this work, we will systematically study the effect of Ni doping on the formation and migration of oxygen vacancies in SrFe$_{1-x}$Ni$_x$O$_{3-\delta}$ and reveal relevant mechanisms.

[a]School of Physics, Hangzhou Normal University, Hangzhou, Zhejiang 311121, China. E-mail: tjia@hznu.edu.cn

[b]Key Laboratory of Materials Physics, Institute of Solid State Physics, HFIPS, Chinese Academy of Sciences, Hefei, 230031, China

[c]Science Island Branch of Graduate School, University of Science and Technology of China, Hefei, 230026, China

2. Methods

All calculations were performed within the Vienna *ab initio* simulation package (VASP)[27–29] and projector-augmented wave

(PAW) method[30] based on density functional theory (DFT). The spin-polarized Perdew–Burke–Ernzerhof generalized gradient approximation (PBE-GGA)[31] was used for the exchange-correlation potential. The plane-wave basis set was converged at a cutoff energy of 450 eV. To account for the strong electron correlations of Fe and Ni ions, we employed the generalized gradient approximation plus Hubbard U (GGA + U) method[32] with $U = 4$ eV (6 eV) for Fe (Ni) 3d electrons. The parent structure of SrFeO$_3$ (SFO) with a cubic lattice constant of 3.857 Å was selected from the experimental results.[33] A $2\sqrt{2} \times 2\sqrt{2} \times 2$ supercell with 80 atoms was used to build the Ni doping systems. We substitute 1, 2, 3, or 4 Fe by Ni in the 80 atom supercell symmetrically, corresponding to SrFe$_{0.9375}$Ni$_{0.0625}$O$_3$ (SFN$_{0.0625}$), SrFe$_{0.875}$Ni$_{0.125}$O$_3$ (SFN$_{0.125}$), SrFe$_{0.8125}$Ni$_{0.1875}$O$_3$ (SFN$_{0.1875}$), and SrFe$_{0.75}$Ni$_{0.25}$O$_3$ (SFN$_{0.25}$) in Fig. 1. The substitution Ni atoms are located at the coordinate (0, 0.75, 0.75) in SFN$_{0.0625}$, coordinates (0.75, 0.5, 0.25) and (0.25, 0, 0.25) in SFN$_{0.125}$, coordinates (0.25, 0.5, 0.25), (0.25, 0, 0.75), and (0.75, 0.5, 0.75) in SFN$_{0.1875}$, and coordinates (0.25, 0.5, 0.25), (0.25, 0, 0.75), (0.75, 0.5, 0.75) and (0.75, 0, 0.25) in SFN$_{0.25}$. A k-point mesh of $3 \times 3 \times 5$ generated by the Monkhorst–Pack scheme[34] was used for the $2\sqrt{2} \times 2\sqrt{2} \times 2$ supercell. To maintain a cubic shape cell but restore FeO$_6$ octahedron distortion, the structural optimization was performed iteratively between the atomic positions relaxation and volume relaxation,[35,36] where we used a Methfessel–Paxton Fermi-level smearing with a width of 0.2 eV. The total energy was converged within 10^{-4} eV per atom and the Hellmann–Feynman force on each atomic site was converged to within 0.01 eV Å^{-1}. Oxygen migration paths and barriers were determined using the climbing image-nudged elastic band (CI-NEB) method,[37] where three intermediate images with the distance about 0.68 Å and a force tolerance of 0.03 eV Å^{-1} were used to determine the minimum energy pathway.

Based on the fully relaxed $2\sqrt{2} \times 2\sqrt{2} \times 2$ (80 atoms, 16 formula unit) supercell in Fig. 1, structures with an oxygen vacancy (V$_O$) was created by removing one neutral oxygen atom, corresponding to an oxygen nonstoichiometry of $\delta = 0.0625$. Since structures with relatively low V$_O$ concentrations have similar lattice parameters to that without V$_O$, the lattice parameters of the oxygen nonstoichiometry cell were fixed at the value of stoichiometric supercell, whereas all atomic positions were fully relaxed. The formation energy E_f of V$_O$ was calculated according to

$$E_f = E_{def} - E_{perf} + \frac{1}{2}[E(O_2) + \Delta h] \tag{1}$$

where E_{def} and E_{perf} are the total energy of the oxygen-deficient and the perfect (stoichiometric) supercells, respectively. $E(O_2)$ is the total energy of an isolated O$_2$ molecule in its triplet ground state and Δh is a correction factor of 1.36 eV per O$_2$ for the oxygen over-binding error addressed by Wang *et al.* for PBE functionals.[38]

To further consider the thermal and vibrational effects, the feasibility of oxygen removal from the perovskites is considered by the temperature and pressure dependent E_f or the free energy of V$_O$ formation:

$$\Delta G_{O_2}(T, P) = \Delta G_{O_2}(P_0) + k_B T \ln \frac{P}{P_0} \tag{2}$$

where

$$\Delta G_{O_2}(P_0) = 2E_f + \Delta G_{O_2}(P_0, T) = 2E_f + [\Delta H_{O_2}(P_0, T) - TS_{O_2}(P_0, T)] \tag{3}$$

The enthalpy $\Delta H_{O_2}(P_0, T)$ and entropy $S_{O_2}(P_0, T)$ of O$_2$ at P_0 (0.1 MPa) are obtained from the JANAF thermochemical tables.[39] Here, the thermal and vibrational contributions from solid SrFe$_{1-x}$Ni$_x$O$_3$ and SrFe$_{1-x}$Ni$_x$O$_{3-\delta}$ were neglected because they
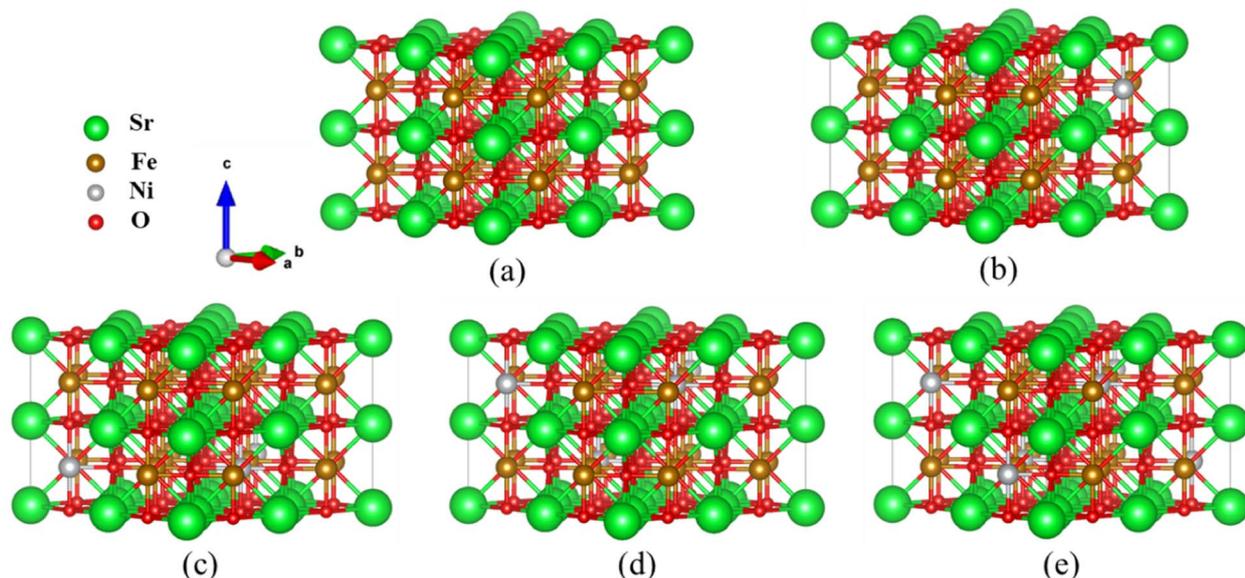

Fig. 1 Optimized $2\sqrt{2} \times 2\sqrt{2} \times 2$ supercell for (a) SFO, (b) SFN$_{0.0625}$, (c) SFN$_{0.125}$, (d) SFN$_{0.1875}$, and (e) SFN$_{0.25}$.

are mostly canceled and negligible compared with O_2 gas. The variation of $\Delta G_{O_2}(P_0)$ on temperature is depicted by an Ellingham diagram.[40]

3. Results and discussion

3.1 Oxygen vacancy formation

A crucial factor that governs the redox performance of oxygen carriers is the extent of oxygen vacancies. Oxygen vacancy formation energy provides insights into the ease of oxygen removal and refilling. Thus, we calculated the oxygen vacancy formation energy for the Ni doping systems $SrFe_{1-x}Ni_xO_3$ ($x = 0$, 0.0625, 0.125, 0.1875, and 0.25), as shown in Table 1. Firstly, we noticed that the lattice constants of $SrFe_{1-x}Ni_xO_3$ decreased very little (or showed nearly no change) with the increase of Ni doping. Normally, the lattice constants should decrease more significantly with Ni doping than with Co doping, due to the tetravalent ionic radius of Ni^{4+} (0.480 Å) < Co^{4+} (0.530 Å) < Fe^{4+} (0.585 Å). Therefore, the doping Ni ions may not be tetravalent here.

To calculate the formation energy E_f of V_O for $SrFe_{1-x}Ni_xO_{3-\delta}$ ($x = 0$, 0.0625, 0.125, 0.1875, and 0.25, $\delta = 0.0625$), a single O atom should be removed from all the studied systems. Due to both B-site substitution and structural distortion, the lowered symmetry results in nonequivalent O sites along Fe–O–Fe or Ni–O–Fe chains. Therefore, we exhaustivly sampled V_O from all nonequivalent O sites, defined as the distances of Fe–O (Ni–O) and O–Fe above 0.01 Å. The nonequivalent O sites for each doping system and the corresponding E_f values are shown in Table 1. In the same Ni doping content, the E_f of V_O from the Ni–O–Fe chains is obviously smaller than that from Fe–O–Fe chains. Besides, the E_f generally decreased as the Ni content changed from $x = 0$ to $x = 0.25$. These trends suggest that Ni doping promotes V_O formation and even has an advantage over Co doping.[23]

Then, we explored the origin of the Ni doping effect on V_O formation and the reason that Ni doping shows a better performance than Co doping. As we know, there are several mechanisms for the promotion of V_O formation.[16] Firstly, we noticed that the the E_f of V_O from Ni–O–Fe chains is lower than that from Fe–O–Fe chains (Table 1). We divided E_f into two terms of the Fe (Ni)–O bonding and relaxation contributions $E_f = E_{bond} + E_{relax}$, where E_{bond} is the energy needed to remove an O from the stoichiometric structure, E_{relax} is the energy obtained from further structural relaxation in the presence of V_O. As shown in Table 1, E_{bond} shows the same trend with E_f that E_{bond} of V_O from Ni–O–Fe chains is lower than that from Fe–O–Fe chains, while the E_{relax} is comparable for V_O from either Ni–O–Fe or Fe–O–Fe chains. Therefore, the weakened Ni–O–Fe bond strength upon Ni doping is one of the key factors to promote V_O formation. Comparatively, Co doping has little influence on the Co–O–Fe or Fe–O–Fe bond strength.[23]

To further understand the mechanism of the Ni-doping induced E_f decrease, we analyzed the density of states (DOS) projected on the Sr, Fe, Ni, and O ions for $SrFe_{1-x}Ni_xO_3$ ($x = 0$, 0.0625, 0.125, 0.1875, and 0.25) shown in Fig. 2(a). For the parent $SrFeO_3$ system, the hybridized Fe–O orbitals form a broad conduction band crossing the Fermi level, conforming to the metallic nature of this compound. The majority of the spin states of Fe are mostly occupied while the minority spin states are nearly unoccupied, reflecting a high spin ($t_{2g}^3 e_g^1$, $S = 2$) Fe^{4+}. The orbitals induced by Ni doping are also hybridized with O-2p bands and are located near the Fermi level with Fe–O hybridization states. With the increase of the Ni doping value, the hybridization or O-2p states near the Fermi level are increased. This change is similar to Co doping[23] which can decrease E_f of V_O and thus promote the V_O formation, since the increased O-2p states near the Fermi level can reduce the spatial and energetic redistribution energy needed at V_O formation.

If we take a closer look at the DOS of Ni ion (shown in the bottom inset of Fig. 2(a)), its majority spin states are fully occupied and minority spin states are partially occupied, indicating a more possible high-spin Ni^{3+} ($t_{2g}^5 e_g^2$, $S = 3/2$) than low spin Ni^{4+} ($t_{2g}^6 e_g^0$, $S = 0$).[41] The exchange splitting of Fe^{4+} is larger than the high-spin

Table 1 The lattice constants a (Å), the distances of Fe–O (Ni–O) and O–Fe in Fe–O–Fe (Ni–O–Fe) chains to create V_O [Fe-V_O (Ni-V_O), V_O-Fe (Å)] and the formation energies E_f (eV), bond energies E_{bond} (eV) and structural relaxation energies E_{relax} (eV) for $SrFe_{1-x}Ni_xO_{3-\delta}$ ($x = 0$, 0.0625, 0.125, 0.1875, and 0.25) by GGA (GGA + U)

x	a (Å)	Fe-V_O (Ni-V_O), V_O-Fe (Å)	E_f (eV)	E_{bond} (eV)	E_{relax} (eV)
0	3.841	1.920, 1.920	2.102 (2.155)	3.162	−1.060
0.0625	3.840	(1.955), 1.871	1.760	2.674	−0.914
		(1.972), 1.868	1.531 (2.174)	2.605	−1.074
		1.936, 1.903	1.860	2.960	−1.100
		1.926, 1.913	1.901	2.997	−1.096
		1.925, 1.929	1.965	2.979	−1.014
0.125	3.839	(1.966), 1.873	1.705 (1.774)	2.677	−0.972
		1.933, 1.906	1.779	2.897	−1.118
		1.924, 1.915	1.809	2.929	−1.120
0.1875	3.839	(1.963), 1.876	1.606	2.594	−0.988
		(1.951), 1.871	1.578 (1.824)	2.516	−0.938
		1.926, 1.913	1.716	2.817	−1.101
		1.941, 1.900	1.725	2.808	−1.083
		1.935, 1.922	1.665	2.788	−1.123
0.25	3.838	(1.956), 1.881	1.293 (1.817)	2.381	−1.088
		1.918, 1.920	1.554	2.926	−1.372

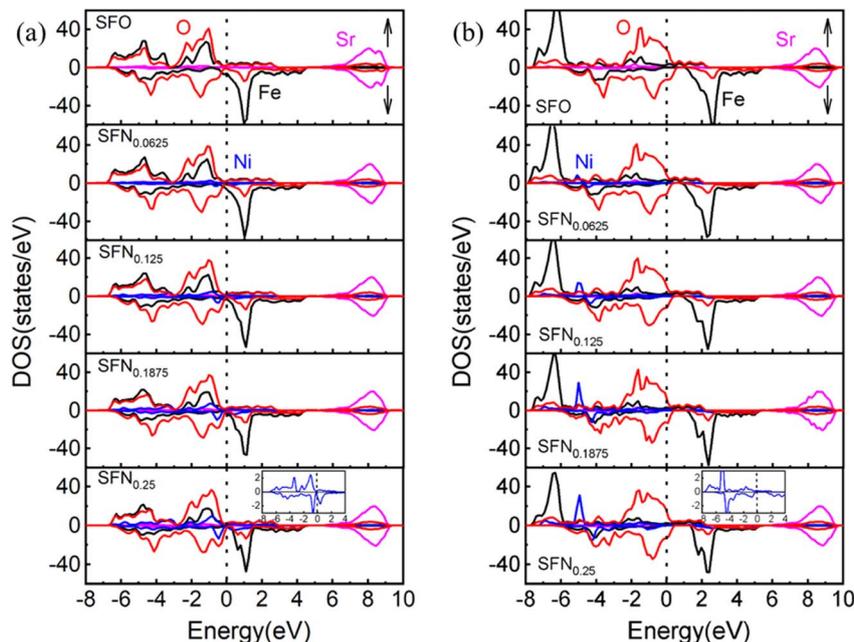**Fig. 2** The partial DOS of $SrFe_{1-x}Ni_xO_{3-\delta}$ ($x = 0$, 0.0625, 0.125, 0.1875, and 0.25) by (a) GGA and (b) GGA + U. The Fermi level (dotted line) is set at 0 eV. Bottom inset: the enlarged DOS for Ni ion.

Ni^{3+}, corresponding to the aforementioned DOS change upon Ni doping that the hybridization states of Ni–O are closer to the Fermi level than that of Fe–O. In addition, the ionic radius of high-spin Ni^{3+} is 0.60 Å, which is comparable with the ionic size of Fe^{4+} (0.585 Å). Again, this provides a reasonable explanation for the little decrease of the lattice constants upon Ni doping. Besides, from the relaxed distances of Ni–O–Fe in Table 1, the Fe–O bond lengths are always shorter than the Ni–O bond lengths in all the Ni doping systems. These results also indicate that the Fe ions have a higher charge state, a smaller ionic radius, and a stronger p–d covalency than the Ni ions. Therefore, our results have consistently suggested a high-spin Ni^{3+} in $SrFe_{1-x}Ni_xO_3$. However, due to the small Ni doping here, the orbital characteristics of Fe^{4+} ions show little change and thus Fe^{4+} in $SrFe_{1-x}Ni_xO_3$ are not changed to Fe^{5+} along with Ni^{3+} as found in $SrFe_{0.5}Ni_{0.5}O_3$.[41] Whereas, the holes introduced by Ni^{3+} substitution would cause a change in cation stoichiometry and hence an imbalance in the net charge. The tendency of compensation to maintain the overall electrical neutrality would withdraw charge from the oxygen sublattice and thus promote the generation of V_O. Thus far, we have identified three factors causing the Ni-doping induced E_f decrease: (1) the weakened Ni–O bonding, (2) moving the O-2p states to the Fermi level by Ni–O hybridization, (3) Ni^{3+} decreasing the positive charges to be compensated by V_O formation. For these reasons, Ni doping has an advantage over Co doping in terms of enhancing the oxygen carrier performance of $SrFeO_{3-\delta}$.

To explore the effects of the onsite Coulomb interactions on the electronic structures, the DOS calculated by GGA + U is shown in Fig. 2(b). The bonding–antibonding splitting of the Fe/Ni 3d bands is significantly enhanced such that the bonding states of Fe (Ni) ions are pushed downwards to about −6 (−5) eV. In the minority spin, the 3d bands of Fe/Ni move

upwards slightly. The antibonding states near the Fermi level are mainly composed of O-2p states. Consequently, the Ni–O hybridization induced O-2p states closing to the Fermi level is weakened in GGA + U. Due to the lack of this factor, the E_f of Ni doping phases calculated by GGA + U is generally larger than that calculated by GGA. As shown in Table 1, the V_O configuration with the lowest E_f for each Ni doping value is calculated by GGA + U. Unlike the gradual decreases of E_f upon Ni doping in GGA, the E_f by GGA + U shows an abrupt decrease when the Ni content increases to $x = 0.125$. Nevertheless, the conclusion of Ni doping promoting V_O formation from GGA and GGA + U is consistent.

3.2 Thermodynamic properties of oxygen storage/release

In experiments, it is impossible to measure the oxygen vacancy formation energy. Instead, oxygen partial pressures and temperatures are used to quantitatively determine the experimental conditions. Therefore, the dependence of free energy for the oxygen release reaction $SrFe_{1-x}Ni_xO_3 \rightarrow SrFe_{1-x}Ni_xO_{3-\delta} + O_2$ on the oxygen partial pressure (P_{O_2}) and temperature (T) is portrayed in Fig. 3. The variation of Gibbs free energy (ΔG) *versus* T can be obtained by using the thermodynamic eqn (3), where E_f for each Ni doping system is an averaged E_f value of $SrFe_{1-x}Ni_xO_{3-\delta}$ ($\delta = 0.0625$) calculated by GGA from Table 1. As shown in Fig. 3(a), this so-called Ellingham diagram at an oxygen partial pressure of 0.1 MPa is commonly applied to compare the free energies of oxygen formation as a function of T. The generally decreasing trend of E_f in Table 1 is well expressed in that the oxygen release temperature is decreased with increased Ni doping. However, the $SrFe_{1-x}Ni_xO_3$ systems are still thermodynamically stable ($\Delta G > 0$) when the
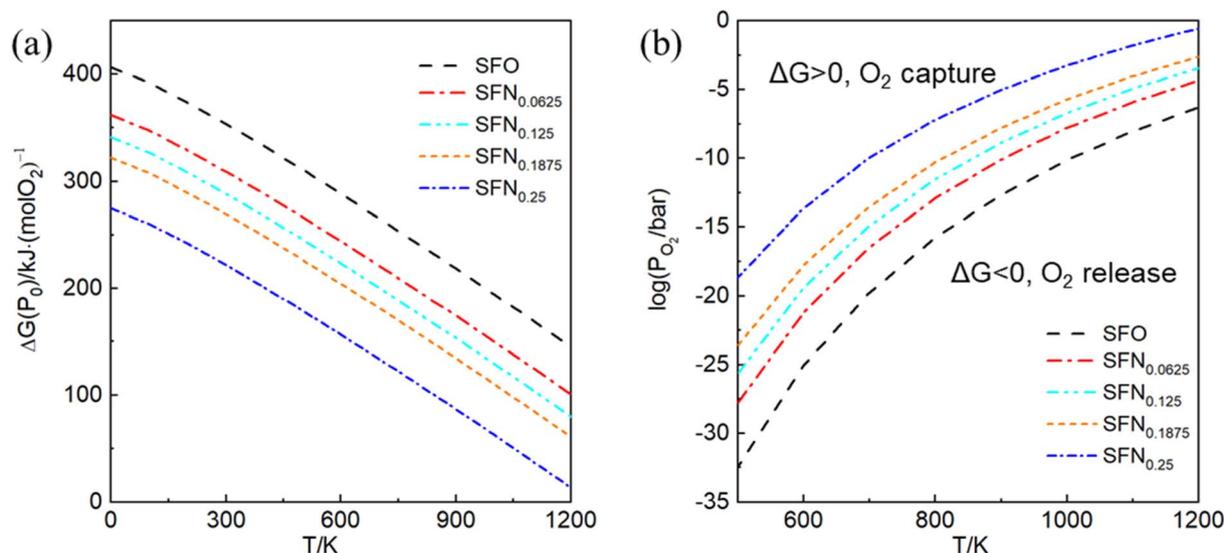
Fig. 3 (a) The Ellingham diagram, (b) counterplotting of ΔG vs. the O_2 pressure and temperature of $SrFe_{1-x}Ni_xO_{3-\delta}$ ($x = 0$, 0.0625, 0.125, 0.1875, and 0.25).

temperature is higher than 1200 K, which means that the oxygen release will not occur spontaneously at $T < 1200$ K. Then, based on eqn (2), the dependence of ΔG on P_{O_2} and T is shown in Fig. 3(b), where only the equilibrium curve ($\Delta G = 0$) is explicitly plotted. The equilibrium curves separate the diagram into two parts: below the line, oxygen will be released from $SrFe_{1-x}Ni_xO_3$ ($\Delta G < 0$, reduction); above the line, oxygen will be captured by $SrFe_{1-x}Ni_xO_{3-\delta}$ ($\Delta G > 0$, oxidation). Therefore, the oxygen release will occur at low O_2 pressure and high temperature. The capability of oxygen release is still increased upon Ni doping. Compared with the Co-doping effect on the oxygen release from $SrFe_{1-x}Co_xO_{3-\delta}$ (Fig. 4 in ref. 23), a little Ni doping $x = 0.25$ can induce a higher P_{O_2} and a lower T than a relatively large Co doping $x = 0.5$.

3.3 Oxygen ion migration

The energy barrier of oxygen migration is another important factor in oxygen carrier performance. In $ABO_{3-\delta}$ perovskites, oxygen migration occurs by hopping to the nearby V_O site, which should pass through a "critical triangle" formed by one B-site cation and two A-site cations (as shown in Fig. 4). For $SrFe_{1-x}Ni_xO_{3-\delta}$, Sr is the only A site element, while B-site cation could be Fe or Ni. Thus, there are at least two pathways for SrSrFe and SrSrNi (Fig. 4(b)). However, the possible diffusion pathways of oxygen are not only distinguished by the variation of the surrounding B-site cation configuration but also by the nonequivalent Fe–O or Ni–O bond length in the structural distortion. Considering these two factors, we calculated oxygen migration barriers for all possible pathways in $SrFe_{1-x}Ni_xO_{3-\delta}$. As shown in Fig. 4(c), the migration barriers generally have a higher value with the B site of Ni than Fe in each doping configuration. The one exception is a slightly higher value with a B site of Fe than Ni in $x = 0.125$ doping configuration, so the difference of detailed barrier energies for each Ni doping value

is also related to their own local distortion. In general, Ni doping increases the migration barrier and thus hinders oxygen migration.
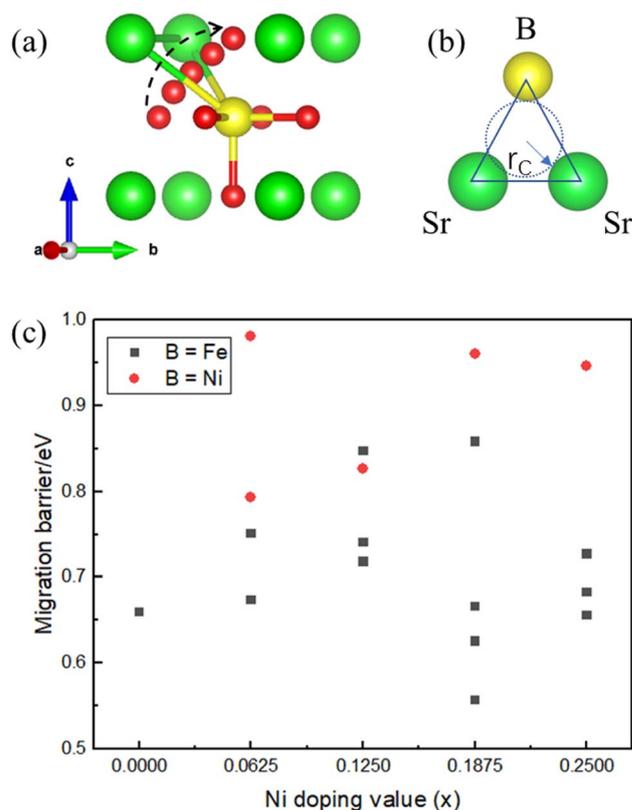

Fig. 4 Schematic diagrams of (a) the oxygen migration path in $SrFe_{1-x}Ni_xO_{3-\delta}$ through the (b) bottleneck of a triangle composed of B-site (Fe or Ni) and two Sr cations. (c) The corresponding oxygen migration barrier for $SrFe_{1-x}Ni_xO_{3-\delta}$ ($x = 0$, 0.0625, 0.125, 0.1875, and 0.25).

Then, we related the trend of the migration barrier with the migration bottleneck, which is the "critical triangle" formed by SrSrFe or SrSrNi (Fig. 4(b)). The bottleneck radius r_C is determined by the lattice constant and the ionic radii of A-site and B-site cations.[42] The migration bottleneck is a rough method used to understand the tendency of migration barriers, since the lattice constant is an averaged reflection of bond properties and the specific barrier values also rely on the local distortion. Usually, a larger r_C value gives rise to a smaller migration barrier. Since the lattice constants of $SrFe_{1-x}Ni_xO_3$ are nearly the same from Table 1 and A-site is only Sr, r_C would be distinguished by the ionic radii of B-site cations Fe/Ni. If we use the tetravalent ionic radius of Fe^{4+} (0.585 Å) and Ni^{4+} (0.480 Å), the corresponding r_C values would be 1.032 and 1.067. It means that the bottleneck of SrSrNi is larger than SrSrFe and thus the migration barriers should have a lower value with the B site of Ni than Fe, which is inconsistent with our barrier results in Fig. 4(c). Whereas, if the ionic radius of Ni is the aforementioned high-spin Ni^{3+} (0.60 Å), the r_C value of SrSrNi is 1.027, which is smaller than that of SrSrFe. The tendency of migration barriers is reasonable. Therefore, the conclusion of a high-spin Ni^{3+} in $SrFe_{1-x}Ni_xO_3$ is reversely verified by the migration barrier results.

Here, we used a small amount of Ni-doped Fe, in which Ni is surrounded by Fe even in the $x = 0.25$ doping system, thus the oxygen hopping can always find a nearby pathway of SrSrFe with a low migration barrier. Therefore, although the pathway of SrSrNi induced by Ni doping is averse to oxygen migration, there would be little impact on the overall oxygen ion conduction for the little Ni doping systems.

4. Conclusions

In conclusion, we have studied the formation and migration of oxygen vacancies in $SrFe_{1-x}Ni_xO_{3-\delta}$ ($x = 0$, 0.0625, 0.125, 0.1875, and 0.25) perovskites. The E_f calculation results show that V_O forms more easily from Ni–O–Fe chains than Fe–O–Fe chains and E_f generally decreases as Ni content increases, reflecting that Ni doping can promote V_O formation. This Ni-promoted formation of V_O results from three factors: weakened Ni–O bonding, the closing O-2p states to the Fermi level by Ni–O hybridization, and the Ni^{3+} decreasing the positive charges to be compensated by V_O formation. Due to the influence of these multiple factors, Ni doping has an advantage over Co doping in the promotion of V_O formation. Thermodynamically, the Ellingham diagram shows that a little Ni doping $x = 0.25$ can induce a higher P_{O_2} and a lower T than relatively large Co doping $x = 0.5$. Kinetically, the oxygen migration pathway of SrSrNi has a higher energy barrier than that of SrSrFe. Considering that the oxygen hopping can always find a nearby pathway of SrSrFe with a low migration barrier in a system with a small amount of Ni doping, the overall oxygen ion conduction would be little influenced. Therefore, a small amount of Ni doing can significantly improve the oxygen carrier performance of the parent $SrFeO_3$ system and promote its application in energy storage, catalysis, gas sensing, chemical looping, *etc.*

Conflicts of interest

There are no conflicts to declare.

References

1 J. Dou, E. Krzystowczyk, X. Wang, T. Robbins, L. Ma, X. Liu and F. Li, *ChemSusChem*, 2020, **13**, 385–393.

2 E. Krzystowczyk, X. Wang, J. Dou, V. Haribal and F. Li, *Phys. Chem. Chem. Phys.*, 2020, **22**, 8924–8932.

3 Y. Yoshiyama, S. Hosokawa, M. Haneda, M. Morishita, H. Asakura, K. Teramura and T. Tanaka, *ACS Appl. Mater. Interfaces*, 2023, **15**, 5293–5300.

4 D. Yu, L. Wang, C. Zhang, C. Peng, X. Yu, X. Fan, B. Liu, K. Li, Z. Li and Y. Wei, *ACS Catal.*, 2022, **12**, 15056–15075.

5 J. Hombo, Y. Matsumoto and T. Kawano, *J. Solid State Chem.*, 1990, **84**, 138–143.

6 J. Mizusaki, M. Okayasu, S. Yamauchi and K. Fueki, *J. Solid State Chem.*, 1992, **99**, 166–172.

7 Y. Takeda, K. Kanno, T. Takada, O. Yamamoto, M. Takano, N. Nakayama and Y. Bando, *J. Solid State Chem.*, 1986, **63**, 237–249.

8 C. Y. Lau, M. T. Dunstan, W. Hu, C. P. Grey and S. A. Scott, *Energy Environ. Sci.*, 2017, **10**, 818–831.

9 J. Vieten, B. Bulfin, D. E. Starr, A. Hariki, F. M. F. de Groot, A. Azarpira, C. Zachäus, M. Hävecker, K. Skorupska, N. Knoblauch, M. Schmücker, M. Roeb and C. Sattler, *Energy Technol.*, 2019, **7**, 131–139.

10 E. Marek, W. Hu, M. Gaultois, C. P. Grey and S. A. Scott, *Appl. Energy*, 2018, **223**, 369–382.

11 S. Brendelberger, J. Vieten, M. J. Vidyasagar, M. Roeb and C. Sattler, *Sol. Energy*, 2018, **170**, 273–279.

12 J. Dou, E. Krzystowczyk, X. Wang, T. Robbins, L. Ma, X. Liu and F. Li, *ChemSusChem*, 2020, **13**, 385–393.

13 G. Luongo, F. Donat and C. R. Müller, *Phys. Chem. Chem. Phys.*, 2020, **22**, 9272–9282.

14 E. J. Popczun, T. Jia, S. Natesakhawat, W. Xu, C. M. Marin, Y. Duan and J. W. Lekse, *J. Alloys Compd.*, 2022, **896**, 162783.

15 J. Vieten, B. Bulfin, P. Huck, M. Horton, D. Guban, L. Zhu, Y. Lu, K. A. Persson, M. Roeb and C. Sattler, *Energy Environ. Sci.*, 2019, **12**, 1369–1384.

16 T. Jia, E. J. Popczun, J. W. Lekse and Y. Duan, *Appl. Energy*, 2021, **281**, 116040.

17 N. Miura, H. Ikeda and A. Tsuchida, *Ind. Eng. Chem. Res.*, 2016, **55**, 3091–3096.

18 S. Chen, H. Cheng, Y. Liu, X. Xiong, Q. Sun, X. Lu and S. Li, *Phys. Chem. Chem. Phys.*, 2021, **23**, 27266–27272.

19 Y. Han, J. Yi and X. Guo, *Solid State Ionics*, 2014, **267**, 44–48.

20 J. Zhu, S. Guo, Z. Chu and W. Jin, *J. Mater. Chem. A*, 2015, **3**, 22564–22573.

21 A. Demizu, K. Beppu, S. Hosokawa, K. Kato, H. Asakura, K. Teramura and T. Tanaka, *J. Phys. Chem. C*, 2017, **121**, 19358–19364.

22 F. Fujishiro, N. Oshima, N. Kamioka, T. Sakuragi and M. Oishi, *J. Solid State Chem.*, 2020, **283**, 121152.

23 T. Jia, E. J. Popczun, J. W. Lekse and Y. Duan, *Phys. Chem. Chem. Phys.*, 2020, **22**, 16721–16726.

24 H.-Y. Su and K. Sun, *J. Mater. Sci.*, 2015, **50**, 1701–1709.

25 M. T. Curnan and J. R. Kitchin, *J. Phys. Chem. C*, 2014, **118**, 28776–28790.

26 A. A. Emery and C. Wolverton, *Sci. Data*, 2017, **4**, 170153.

27 G. Kresse and J. Furthmuller, *Comput. Mater. Sci.*, 1996, **6**, 15–50.

28 G. Kresse and J. Furthmuller, *Phys. Rev. B: Condens. Matter Mater. Phys.*, 1996, **54**, 11169–11186.

29 G. Kresse and J. Hafner, *Phys. Rev. B: Condens. Matter Mater. Phys.*, 1993, **47**, 558–561.

30 P. E. Blöchl, *Phys. Rev. B: Condens. Matter Mater. Phys.*, 1994, **50**, 17953–17979.

31 J. P. Perdew, K. Burke and M. Ernzerhof, *Phys. Rev. Lett.*, 1996, **77**, 3865–3868.

32 S. L. Dudarev, G. A. Botton, S. Y. Savrasov, C. J. Humphreys and A. P. Sutton, *Phys. Rev. B: Condens. Matter Mater. Phys.*, 1998, **57**, 1505–1509.

33 P. Manimuthu and C. Venkateswaran, *J. Phys. D: Appl. Phys.*, 2011, **45**, 015303.

34 H. J. Monkhorst and J. D. Pack, *Phys. Rev. B: Solid State*, 1976, **13**, 5188–5192.

35 Y.-L. Lee, Y. Duan, D. Morgan, D. C. Sorescu, H. Abernathy and G. Hackett, *Phys. Rev. Appl.*, 2017, **8**, 044001.

36 Y.-L. Lee, J. Kleis, J. Rossmeisl and D. Morgan, *Phys. Rev. B: Condens. Matter Mater. Phys.*, 2009, **80**, 224101.

37 G. Henkelman, B. P. Uberuaga and H. Jónsson, *J. Chem. Phys.*, 2000, **113**, 9901–9904.

38 L. Wang, T. Maxisch and G. Ceder, *Phys. Rev. B: Condens. Matter Mater. Phys.*, 2006, **73**, 195107.

39 M. W. Chase Jr, *J. Phys. Chem. Ref. Data, Monogr.*, 1998, **9**, 1–1951.

40 H. J. T. Ellingham, *J. Soc. Chem. Ind.*, 1944, **63**, 125–133.

41 F. Fan, Z. Li, Z. Zhao, K. Yang and H. Wu, *Phys. Rev. B*, 2016, **94**, 214401.

42 J. A. Kilner and R. J. Brook, *Solid State Ion.*, 1982, **6**, 237–252.